ELSEVIER

Earth and Planetary Science Letters 160 (1998) 65–80

EPSL

Transportation of H_2O and melting in subduction zones

Hikaru Iwamori *

Department of Earth and Planetary Sciences, Nagoya University, Chikusa, Nagoya, Japan

Received 5 November 1997; accepted 3 May 1998

Abstract

Material recycling in subduction zones, including the generation and migration of aqueous fluids and melts, is key to understanding the origin of volcanism in subduction zones and is also important for understanding the global circulation of materials. Recent knowledge concerning the phase relationships of hydrous peridotitic and basaltic systems allows us to model the fluid generation and migration in subduction zones. Here I present a numerical model, in which the aqueous fluid migrates by permeable flow and interacts chemically with the convecting solid, including melting. The calculation results suggest that nearly all the H_2O expelled from the subducting slab will be hosted by serpentine and chlorite just above the slab, and is brought down by up to 150 km, depending on the temperature along the slab. Breakdown of serpentine and chlorite at these depths results in the formation of a fluid column through which H_2O is transported upwards. The fluid reaches a depth corresponding to a cusp of the H_2O-undersaturated solidus of peridotite (minimum at 2.5 GPa) and initiates extensive melting whose depth and the lateral extent toward the trench side is nearly fixed, irrespective of the age of the slab. This is because the flux of H_2O and the depression of the practical solidus temperature in the mantle wedge are similar for models with different slab ages. Exceptionally, for very young slabs (e.g. $\ll$10 Myr when the subduction velocity is $\sim$6 cm/y), different melting regimes occur, such as melting in the forearc region and slab melting. If the aqueous fluid released from the slab migrates upwards in disequilibrium (e.g. through fractures), significant melting occurs in the forearc region, since the serpentinite layer, an effective H_2O-absorber, is not formed. However, this is not the case in most subduction zones. Further studies with various subduction parameters, and melt segregation processes which are not included in this study, are required to compare the model results with the observed distribution and chemistry of arc magmas.

Keywords: melting; water; subduction; fluid phase; migration

1. Introduction

Subduction zones are one of the major sites of volcanism on the Earth, yet the mechanism of melt generation is poorly understood. A significant amount of H_2O is thought to be expelled from the subducting slab and to contribute to melt generation. Introduction of H_2O lowers melting temperatures of rocks (hereafter referred to as 'flux melting'), which can cause melting even in a relatively cool environment. This mechanism has been argued to be important in the mantle wedge of subduction zones by many researchers (e.g. [1,2]).

In order to evaluate the distribution of H_2O in subduction zones, hydrous phase relationships for

* Present address: Geological Institute, University of Tokyo, Hongo 7-3-1, Bunkyo-ku, Tokyo 113-0033, Japan. Tel.: +81-(0)3-3812-2111-4515. Fax: +81-(0)3-3815-9490. E-mail: hikaru@geol.s.u-tokyo.ac.jp

0012-821X/98/$19.00
PII S0012-821X(98)00080-6

basaltic and peridotitic systems have been investigated (e.g. [3–6]). These studies discussed the sequence of dehydration reactions and the amount of expulsion of H_2O along the subducting slab. Tatsumi [3] argued that amphibole in the downward flow of the mantle wedge breaks down to release H_2O, which ascends vertically as fluid (either aqueous solution or H_2O-rich melt) to cause flux melting and formation of a volcanic front. On the other hand, Davies and Stevenson [7] argued that H_2O released from amphibole reacts with peridotites during its ascent to form amphibole again and that H_2O can travel over a significant horizontal distance to a potential melting region. These arguments suggest that transportation of H_2O needs be estimated taking both the relevant reactions and the fluid flows quantitatively into account. Melting associated with movement of a hydrous rock packet (i.e. decompression–compression melting [8–10]) also needs be considered, since convection in the mantle wedge must be occurring.

The main aim of this paper is to propose a model integrating the processes described above: generation and migration of H_2O-rich fluid, interactions of the fluid with the convecting solid, and melt generation in this dynamic situation. First, parameterized phase relationships for peridotite–H_2O and basalt–H_2O systems are presented, based on the data sets from the literature. Second, a numerical model, which describes the migration of H_2O-rich fluid, mantle flow and melting, is presented. Based on the calculation results, the transportation paths, the amount of H_2O, and consequent melting processes are discussed.

2. Phase relationships

The experimental results for melting phase relations in the H_2O-bearing peridotitic systems are compiled in Fig. 1. Below 3 GPa (Fig. 1a), the phases present are olivine, orthopyroxene, clinopyroxene, spinel, garnet, amphibole, melt, and vapour. In several data from Ref. [11], spinel is not reported, although they plot in the spinel stability field. This indicates that some of the experimental results could have attained only partial equilibration. Several minor phases such as phlogopite occur depending on the bulk composition, but are neglected in the following analyses of the phase relationships.

Within the *P–T* and compositional range of interest, the system can be approximated as a SiO_2–(Mg,Fe)O–CaO–Al_2O_3–H_2O system which is saturated with olivine and two-pyroxenes. Therefore, the variable components may be reduced to Al_2O_3–H_2O with five phases, spinel, garnet, amphibole, melt, and vapour, expressed by the symbols S, G, A, M, and V in Fig. 1a, respectively. In this pseudobinary system, each symbol does not correspond to the exact composition of each phase. Components which are not balanced by the reaction among the above five phases should be buffered by olivine + two pyroxenes. It is also noted that the composition of each phase, especially of the melt, changes as the relevant reaction proceeds. Consequently, the reaction takes place over a *P–T* range, although the experimental results suggest that many of these reactions occur within a limited *P–T* range.

This system has three pseudoinvariant points: I1 (G-absent), I2 (V-absent) and I3 (S-absent). The reaction lines I1–I2 and I2–I3 define the H_2O-undersaturated solidus whose position varies with the H_2O content. In Fig. 1(a), the data for 0.09 wt% H_2O, 0.2 wt% and the saturated conditions ($\geq$0.4 wt%) are shown, with the solidus curves for 0.2 wt% and the saturated case. As H_2O increases, the amphibole stability field shrinks to lower the H_2O-undersaturated solidus temperature, and the reaction line G = S + M also shifts with I2 towards a lower temperature. Plagioclase is not reported in the experiments shown in Fig. 1, and its stability field in the hydrous systems is not constrained. Therefore, the reaction lines at low pressures around I1 are shown by dotted lines in Fig. 1.

The line I2–I3 has negative dT/dP, suggesting that the melting reaction produces a denser assemblage, garnet + melt, whereas the melting reaction I1–I2 produces a lighter assemblage, spinel + melt. The line I2–I3 connects to amphibole-breakdown reaction below solidus at 2.2–2.5 GPa [12,6]. Some of the experiments in Fig. 1a and Refs. [13,14] suggest that amphibole could be stable at higher pressure, depending on the bulk composition, e.g. in the presence of CO_2, F or K. However, as long as H_2O is dominant among these components, major breakdown of amphibole occurs at around 2.5 GPa [14].

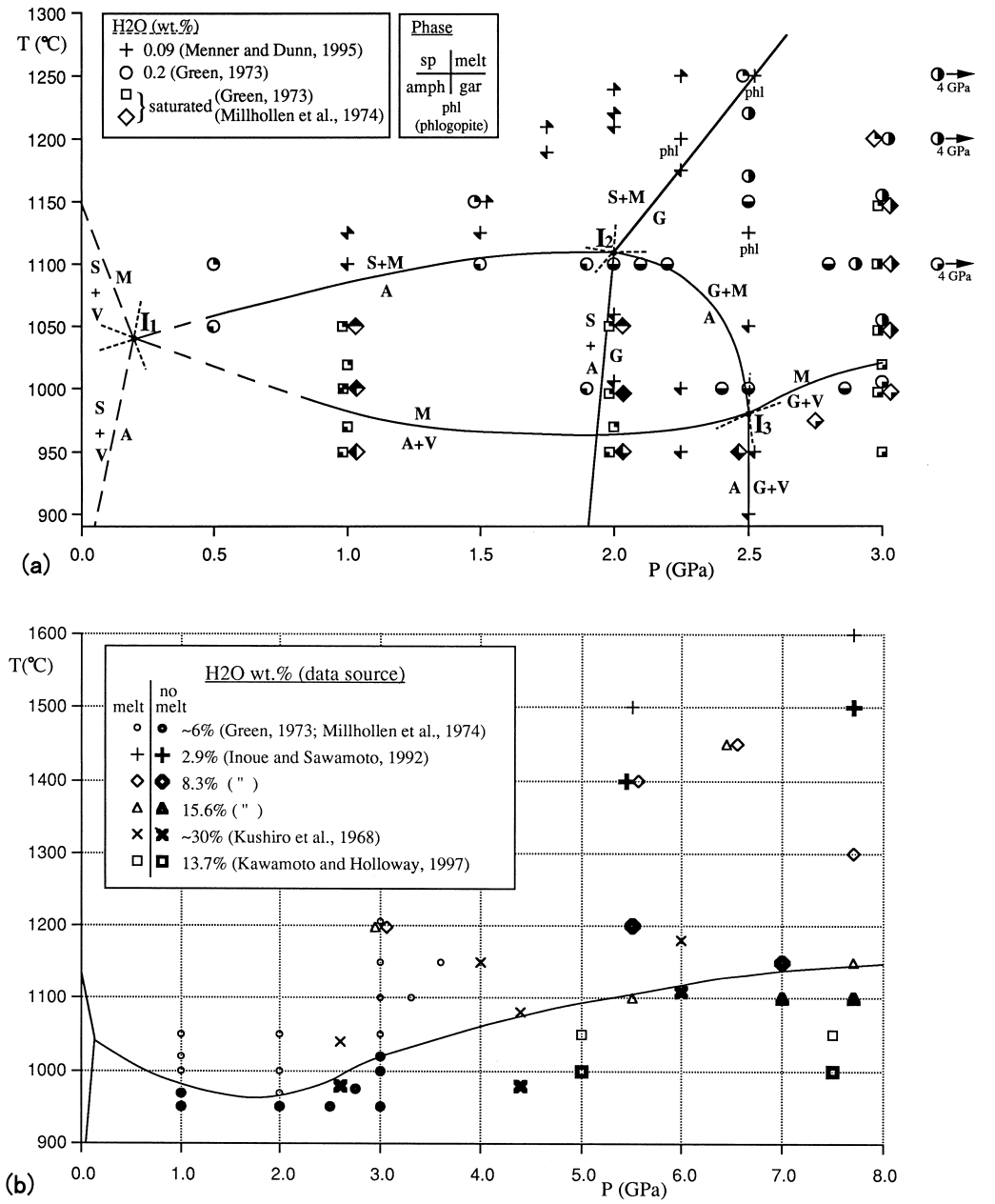

Fig. 1. Melting phase relationships for hydrous peridotite systems, based on the experiments [11,15,16,19,25,34]: (a) <3 GPa for H_2O-undersaturated and saturated conditions, and (b) <8 GPa for H_2O-saturated conditions. For further explanation see text.

Fig. 1b presents the experimental results for H_2O-saturated conditions from 0 to 8 GPa, which show a wide variation in the solidus temperatures above ~3 GPa from different experiments. The variation is partly due to the different chemical compositions of the systems: the MgO contents vary from 32.3% to 39.2% (dry condition). The H_2O contents range from 2.9 to ~30 wt%, with a significant decrease in the solidus temperature with increasing H_2O content: e.g. from 1500°C for 2.9% H_2O

to 1100ºC for 15.6% H_2O at 7.7 GPa for a pyrolite composition in the CaO–MgO–FeO–Al_2O_3–SiO_2 system [15] (Fig. 1b), and 1550 to 1150ºC at 6 GPa for sealed and unsealed runs of the Salt Lake nodule [16]. These runs were H_2O-saturated below the solidus temperatures, except that the unsealed run by Kushiro et al. [16] may not be.

One might expect that if the system is saturated with H_2O, the solidus temperature does not change by the amount of excess-H_2O. However, the vapour phase dissolves a significant amount of silicate components and may even form a single phase with melt at high pressures, continuously changing its composition [17–19]. Also considering that identification of these fluids is difficult, especially when its amount is small, the 'solidus' observed in the experiments probably corresponds to a practical solidus above which a detectable amount (more than a few percent) of silicate melt is formed. Utilizing the practical solidus for modelling of melting processes will give a reasonable approximation in terms of the energy balance, which is the major concern of this paper. It should be noted, however, that the incipient melt is crucial to the chemical behaviour of highly incompatible elements.

In spite of these complications, the H_2O-saturated practical solidus at ~6 GPa for natural peridotites is reported to be less than 1200ºC (Fig. 1b), and is parameterized as in Fig. 2. This curve is similar to the solidus drawn by Thompson [5] and Kushiro et al. [16]. Fig. 2 also shows the major subsolidus reactions after Schmidt and Poli [6], which define the H_2O solubility of the subsolidus assemblages. One of the key subsolidus reactions relates to the stability of serpentine which contains ~12 wt% H_2O (serpentinites of peridotitic compositions can contain more than 6.4 wt% H_2O [6]). Serpentine breaks down to olivine + talc + H_2O (<2 GPa and 500–700ºC), olivine + orthopyroxene + H_2O (2–6 GPa and 700–600ºC), or phase A + orthopyroxene + H_2O above 6 GPa (thick line in Fig. 3). The predicted geotherms of the mantle wedge along the subducting slab can intersect this line at various depths, which causes production of H_2O-fluid (maximum 7 wt% of the system).

Amphibole has been argued to be an important phase to control the distribution of H_2O in the mantle wedge (e.g. [3,7]). Tatsumi [3] suggested that the constant location of the volcanic front can be related to the stability field of amphibole whose dehydration occurs at around 3 GPa, nearly independent of the thermal structure. Of the subsolidus phases, however, amphibole accommodates a relatively small amount of H_2O (~0.4 wt% as amphibole-bearing peridotites [3,6]). Amphibole is, however, nearly the only hydrous phase above about 800ºC and below 2.5 GPa, and controls dehydration melting (Figs. 1 and 2).

The reaction that occurs at the highest temperature in Fig. 2 is melting of the anhydrous peridotite. As the concentration of H_2O increases, the temperatures of the H_2O-undersaturated solidus defined by breakdown of amphibole ($\leq$2.5 GPa) and the practical solidus (>2.5 GPa) decrease, as has been discussed. The solidus curve with 0.2% H_2O has been parameterized as in Fig. 3 based on the experiments compiled in Fig. 1. It should be stressed that there are few data above 3 GPa (only at 4 GPa, Fig. 1a; [11]). Also, above 2.5 GPa, the bulk solubility of H_2O for peridotites is not well constrained, although it is likely to be small, being controlled by phlogopite, K-richiterite and nominally anhydrous minerals. Considering these uncertainties, the practical solidus temperature above 2.5 GPa is assumed not to decrease further when the bulk H_2O content exceeds 0.4 wt%, in order to have smooth connection with the data below 2.5 GPa (Fig. 3a). The solidus for an arbitrary H_2O content is assumed to be given by linear interpolation between the three reference solidi of 0 wt% H_2O, 0.2 wt% and 0.4 wt%. This approximation roughly fits the data for 0.09 wt% H_2O shown in Fig. 1a.

The amount of melt produced at a given pressure and temperature increases with an increasing amount of H_2O. Fig. 3b shows the results of a parameterization for the $T - X - C_{H_2O}$ relationship of peridotite at 1 GPa, based on experiments by Hirose [20] and on a method for parameterization similar to that of Iwamori et al. [21]. When the system is saturated with H_2O, addition of excess-H_2O will produce more melt at the onset of melting until the vapour phase (excess-H_2O) disappears. This behaviour is observed in the experiments by Hirose [20], and is incorporated into the parameterization as is shown in Fig. 3b. Using the parameterization, X is calculated as a function of P, T, and C_{H_2O}.

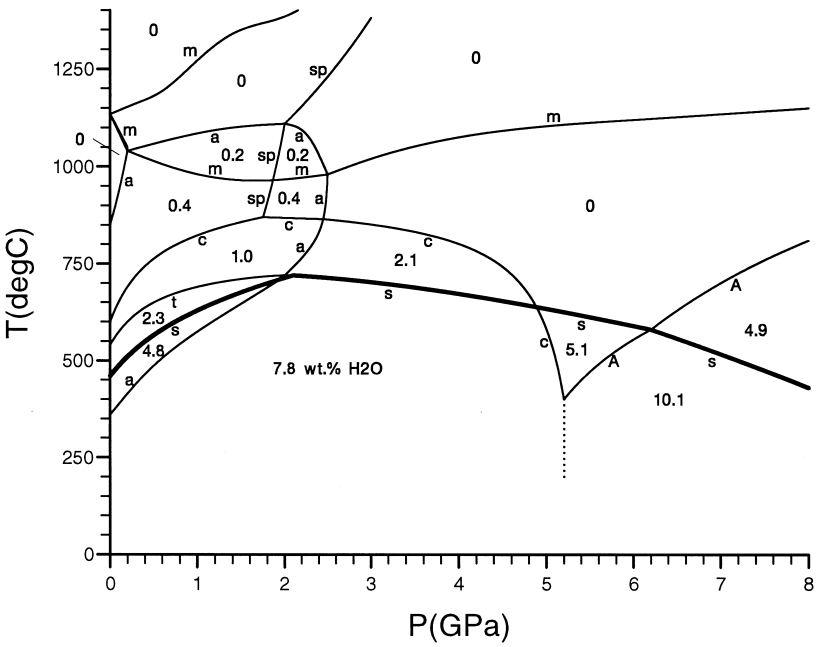

Fig. 2. *P–T* boundaries for major hydration–dehydration reactions, including melting and subsolidus reactions, based on Fig. 1 and Ref. [6]. The melting reactions are described by interpolating the following points by natural cubic spline, as in Ref. [21]. For the H_2O-free solidus curve, the reference pressures are P (GPa) = (0.0, 0.3, 0.6, 0.9, 1.4, 2.0, 3.0, 4.0, 7.0, 10.0, 14.0) and the corresponding reference temperatures are T (ºC) = (1134.32, 1161.95, 1193.30, 1251.01, 1339.89, 1383.75, 1533.19, 1644.75, 1781.92, 1869.43, 1932.23), the same as in Ref. [21]. The H_2O-saturated solidus curve consists of three parts: (1) P = (0.0, 0.2) and T = (1134.32, 1050.0) (straight line); (2) P = (0.2, 1.0, 1.85, 2.5) and T = (1040.0, 980.0, 965.0, 980.0); and (3) P = (2.5, 3.0, 6.0, 8.0) and T = (980.0, 1020.0, 1120.0, 1150.0). The subsolidus reaction curves are based on [6]. Each line is labelled with a characteristic phase on its stable side. The abbreviations for the phases are: *a* = amphibole; *s* = serpentine; *t* = talc; *c* = chlorite; *sp* = spinel; *m* = melt; *A* = phase A. The H_2O solubilities (wt%) in each field are also shown, based on [6]. The following reference points are used to describe the lines with rational function interpolation [37]. The reaction lines labelled *a* consist of five parts: (1) P (GPa) = (0.0, 0.3, 0.57, 1.17, 1.88, 1.95) and T = (360.0, 440.0, 500.0, 600.0, 700.0, 710.0); (2) P = (1.95, 2.0, 2.45, 2.5) and T = (710.0, 720.0, 865.0, 980.0); (3) P = (2.0, 2.3, 2.5) and T = (1110.0, 1070.0, 980.0) (by cubic spline); (4) P = (0.2, 1.0, 1.4, 2.0) and T = (1050.0, 1085.0, 1100.0, 1110.0) (by cubic spline); (5) P = (0.0, 0.2) and T = (1040.0, 850.0). The reaction lines labelled *s* consist of three parts: (1) P = (0.0, 0.2, 0.75, 1.95, 2.1) and T = (460.0, 510.0, 600.0, 710.0, 720.0); (2) P = (2.1, 3.1, 4.6, 6.2) and T = (720.0, 700.0, 650.0, 580.0); (3) P = (6.2, 7.2, 8.0) and T = (580.0, 500.0, 430.0). The reaction line labelled *t* is a single curve: P = (0.0, 0.2, 1.0, 2.0, 2.1) and T = (540.0, 600.0, 690.0, 720.0, 720.0), which should be extended to higher pressure. The reaction lines labelled *c* consist of three parts: (1) P = (0.0, 0.2, 0.77, 1.75) and T = (600.0, 690.0, 800.0, 870.0); (2) P = (1.75, 2.45) and T = (870.0, 865.0); (3) P = (2.45, 4.7, 5.2) and T = (865.0, 700.0, 400.0). The reaction lines labelled *sp* consist of two parts: (1) P = (1.75, 2.0) and T = (870.0, 1110.0); (2) P = (2.0, 3.0) and T = (1110.0, 1380.0). The reaction lines labelled *A* consist of two parts: (1) P = (5.3, 5.65, 6.2) and T = (400.0, 500.0, 580.0); (2) P = (6.2, 7.0, 8.0) and T = (580.0, 700.0, 810.0).

3. Water content in the subducting slab

Compared to the peridotitic system, basaltic systems include more H_2O-related reactions, involving chlorite, lawsonite, epidote-zoisite, amphibole, paragonite, chloritoid, talc and phengite [5,6,22]. These numerous reactions with solid solutions cause rather continuous dehydration along the subducting slab [6]. Therefore, the solubility of H_2O of the basaltic portion of the subducting slab is parameterized by a continuous function of pressure and temperature (Fig. 4).

At relatively low pressure and temperature (<400ºC and <2 GPa), more than ~4 wt% H_2O can be retained in the subducting basalt. At around 2.5 GPa, almost independent of temperature, the solubil-

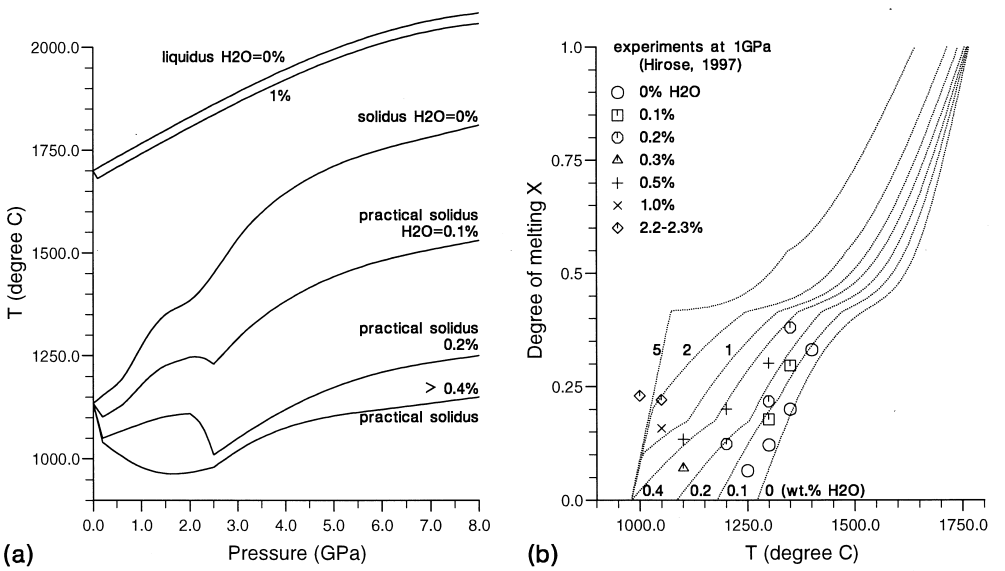

Fig. 3. Parameterized melting behaviours of peridotites for variable pressure (P), temperature (T), and composition (H_2O content). (a) Liquidus and solidus curves, and (b) degree of melting (X). (a) The liquidus and solidus curves are described by interpolating the following points by natural cubic spline, as in Ref. [21]: for H_2O-free liquidus curve, the reference pressures are P (GPa) = (0.0, 7.0, 14.0) and the corresponding reference temperatures are T (ºC) = (1699.67, 2064.24, 2033.35), respectively. The solubility of H_2O, $a_m^{H_2O}$ (wt%), greatly changes with pressure, and is approximated by $27 \times [1 - \exp(-P/2)]$, irrespective of T and compositions, based on Refs. [35,36]. The depression of the liquidus temperature, $(T_l^{dry} - T_l^{hydrous})$, is assumed to be linearly proportional to the amount of H_2O in the melt, $C_m^{H_2O}$, and is expressed by $C_m^{H_2O} \times 25$, based on the experimental results [35,36]. The H_2O-free solidus curve and the H_2O-saturated solidus curve are the same as is defined in the caption of Fig. 2. The solidus curve with 0.2 wt% H_2O consists of four parts: (1) P = (0.0, 0.2) and T = (1134.32, 1050.0) (straight line), (2) P = (0.2, 1.0, 1.4, 2.0) and T = (1050.0, 1085.0, 1100.0, 1110.0), (3) P = (2.0, 2.3, 2.5) and T = (1110.0, 1070.0, 1010.0), and (4) P = (2.5, 3.0, 4.0, 6.0, 8.0) and T = (1010.0, 1050.0, 1120.0, 1210.0, 1250.0). This curve is slightly different from the curve labelled a in Fig. 2, because the former represents the practical solidus curve, whereas the latter is illustrated not to violate the phase rule (see text for details). The numerical calculations have been performed with the practical solidus curve. (b) The relationships between degree of melting and the temperature are obtained based on the experimental results with H_2O content from 0 to 2.3 wt% at 1 GPa for KLB-1 [20]. A parameterization scheme similar to Ref. [21] is used, stretching the H_2O-free T' (homologous temperature)–X relationship between the hydrous solidus and liquidus. In order to reproduce a relatively low $(\partial X/\partial T)_{P,CH_2O}$ near the hydrous solidus temperatures, the degree of melting at $T' = -0.25$ is lowered by a factor W_0: $W_0 = 1 - C \times (1 - 17/27)/0.2$ when $P \geq 1$ GPa, or $W_0 = 1 - C \times (1 - 17/27)/0.2 \times P/P_0$ when $P < 1$ GPa, where C is taken to be $\min(C_{H_2O}, 0.2)$ in wt%, and $P_0 = 1$ GPa. Also in order to reproduce an eutectic like behaviour when H_2O-saturated (i.e. the vapour phase is present), the $T(') - X$ relationship is stretched between the hypothetical solidus temperature that is lower than the true H_2O-saturated solidus and the hydrous liquidus. The hypothetical homologous solidus temperature, T'_{hyp}, is determined by the stretching factor, W_1, as follows: $T'_{hyp} = -0.5 - W_1(C_{H_2O}/0.4 - 1)$ where C_{H_2O} is in wt% and must be ≥ 0.4. W_1 has been determined to fit the experimental results, and is expressed by $W_1 = 0.136 \times \exp(-P/P_0) + 0.02$ when $P \geq 1$ GPa, or $W_1 = (0.136 \times \exp(-1) + 0.02) \times (P/P_0)^{0.2}$ when $P < 1$ GPa. A straight line that extends from the true solidus temperature with a steep dX/dT slope replaces the above curve near the solidus temperature to reproduce an eutectic behaviour. The slope of the straight line, W_2, is arbitrary chosen as 3 which gives that $X = 3 \times (T' + 0.5)$. The cross point between the stretched curve and the straight line above defines the solubility of H_2O into the melt, which roughly corresponds to the solubility change with pressure as was described above.

ity decreases quite quickly with increasing pressure, and lawsonite becomes the major remaining hydrous phase. Between 400 and 600ºC at <2.5 GPa, the solubility decreases greatly as temperature increases, and amphibole becomes the remaining hydrous phase. Note that the slab, except for a very young hot one, is not heated up enough to melt, according to recent numerical calculations (e.g. [7,10]), therefore, melting of the subducting slab is not modelled in this study.

Dehydration of the sediment portion of the oceanic crust also proceeds rather continuously, but may bring H_2O down by Topaz-OH or phase 'egg'

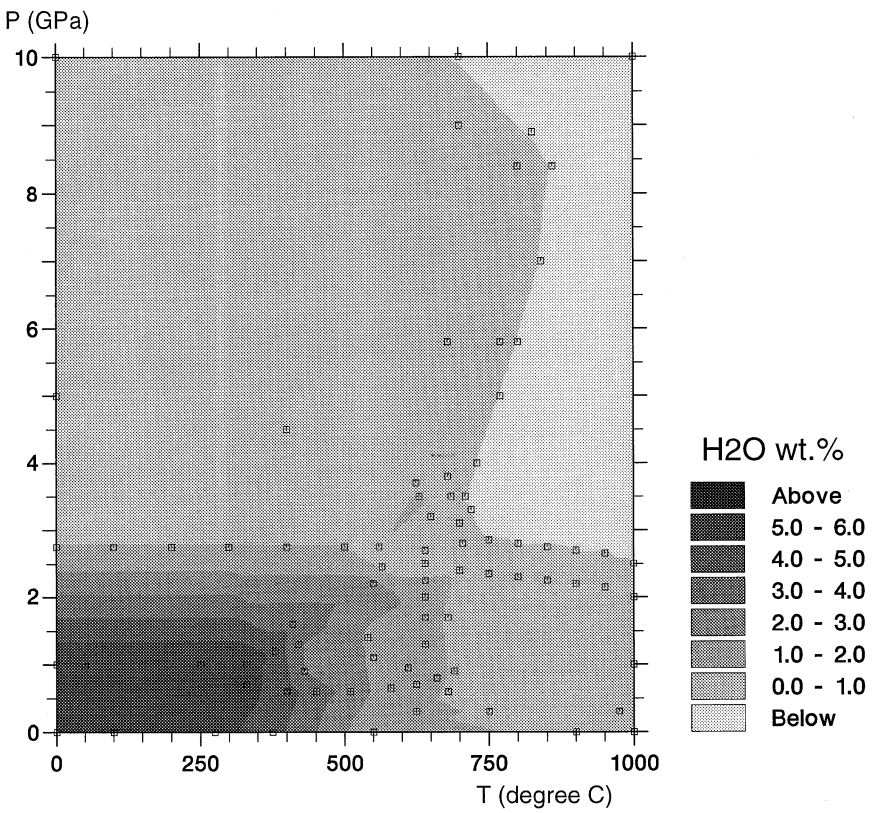

Fig. 4. The solubility of H_2O in a system of a mid-ocean ridge basalt composition, as a continuous function of pressure and temperature, based on Schmidt and Poli [6]. The squares indicate the reference points with which Delaunay triangulation has been used for 2-dimensional linear interpolation over the *P*–*T* space [38]. The reference points are *P* (GPa) = (0.7, 1.0, 1.2, 1.3, 1.6, 0.6, 0.6, 0.9, 0.6, 1.1, 1.4, 2.2, 0.3, 0.6, 0.6, 0.7, 0.8, 0.9, 1.3, 1.7, 2.0, 2.2, 2.8, 3.2, 3.5, 3.7, 2.5, 2.5, 2.7, 2.8, 3.1, 3.8, 3.5, 5.8, 5.8, 8.4, 0.0, 10.0, 10.0, 0.0, 2.8, 2.8, 2.8, 2.8, 2.8, 4.5, 9.0, 1.0, 1.0, 1.0, 3.3, 2.7, 2.7, 2.8, 2.8, 2.8, 5.8, 7.0, 8.4, 8.9, 10.0, 3.5, 10.0, 4.0, 5.0, 2.2, 2.2, 2.2, 2.3, 2.3, 0.3, 2.4, 1.7, 0.9, 0.3, 2.8, 5.0, 1.0, 0.0, 0.0, 0.0, 0.0, 1.0, 2.0, 2.5, 0.0), *T*ºC = (330, 330, 380, 420, 410, 400, 450, 430, 510, 550, 540, 550, 625, 680, 580, 625, 660, 610, 640, 640, 640, 640, 560, 650, 630, 625, 565, 640, 640, 705, 700, 680, 685, 680, 770, 800, 0, 0, 1000, 1000, 100, 200, 300, 400, 500, 400, 700, 50, 150, 250, 720, 950, 900, 850, 800, 750, 800, 840, 860, 825, 700, 710, 700, 730, 770, 900, 950, 850, 800, 750, 750, 700, 680, 690, 975, 0, 0, 0, 100, 375, 550, 900, 1000, 1000, 1000, 275.0) and the corresponding H_2O solubility C_{H_2O} (wt%) = (5.4, 6.0, 4.7, 3.1, 3.8, 4.4, 3.5, 3.0, 2.7, 1.7, 1.9, 2.3, 1.2, 0.9, 1.4, 1.5, 1.2, 1.3, 1.4, 1.8, 1.5, 1.1, 1.0, 0.9, 1.1, 0.9, 0.8, 0.45, 0.5, 0.6, 0.1, 0.45, 0.5, 0.4, 0.1, 0.1, 6.0, 0.4, 0.0, 0.0, 1.0, 1.0, 1.0, 1.0, 1.0, 0.9, 0.1, 6.0, 6.0, 6.0, 0.0, 0.0, 0.0, 0.0, 0.0, 0.0, 0.0, 0.0, 0.0, 0.0, 0.0, 0.0, 0.0, 0.0, 0.0, 0.0, 0.9, 0.9, 0.9, 0.9, 0.9, 0.9, 0.9, 0.9, 0.9, 0.9, 1.0, 0.9, 6.0, 6.0, 4.4, 1.2, 0.9, 0.9, 0.9, 0.0, 5.4).

deeper when compared to the basaltic portion [23]. Also the sediments can be a major source of specific elements or isotopes which characterize the subduction zone magmas (e.g. ^{10}Be). However, assuming that 10% of the oceanic crust consists of sediments, its contribution to the water budget is less than 10% of the basalt, based on the maximum H_2O content of the sediment [23].

Peridotite underlying the oceanic crust is likely to be hydrated to some extent along transform faults and fracture zones, and can bring down a significant amount of H_2O at subduction zones [6]. Since the temperature of the peridotite portion of the subducting slab is lower than that of the oceanic crust and overlying mantle wedge, the hydrated peridotite may retain H_2O down deeper than 300 km by serpentine and phase A, unless the peridotite within the slab is rather hot (i.e. more than 600ºC at 6 GPa, 200 km) ([6] and Fig. 2). Therefore, release of H_2O from the serpentinite underlying the oceanic crust is probably insignificant at depths modelled in this study (<250 km).

4. Model for transportation of H_2O and melting in the mantle wedge

In this model, a subducting slab with a constant velocity and angle is assumed to drive the circulation of the solid in the mantle wedge by dragging. The drag force is thought to be dominant over buoyancy due to the thermal gradient and the presence of melts [7,10], so the circulation of the solid can be described by an analytic corner flow solution [24]. Standard temperature profiles for subduction zones [7,10,25] are set on the side boundaries.

The aqueous fluid present is assumed to migrate as porous flow along the solid grain boundaries, according to the pressure gradient due to the density contrast and the solid flow. The effect of channel flow through sparsely distributed paths, which may cause chemical disequilibrium, will be discussed also. The solid and fluid transport H_2O, which affects the phase relationships (e.g. the local solidus temperature). The phases present (aqueous fluid, melt, solid) and the amount of H_2O in each phase are then calculated according to the parameterized phase relationships and the solubilities of H_2O.

No differential movement between the melt and solid is assumed in this model. If the melt migrates and equilibrates with the solid which it newly encounters, the chemical composition of the local system will be changed. Since the phase relationships for the variable major compositions have not been parameterized, only batch melting in which the composition of the system remains constant will be discussed. In spite of this limitation, the model is useful for investigating the generation and migration of aqueous fluids and their interactions with solid, including the initial stages of melting. Based on these assumptions, conservation of mass, momentum and energy can be written as follows:

$$\frac{\partial(\rho_i\phi_i)}{\partial t} + \nabla\cdot(\rho_i\phi_i\boldsymbol{V}_i) = \sum_{j\neq i}\Gamma_{j\to i}$$

$$\text{and}\quad \sum_i\sum_{j\neq i}\Gamma_{j\to i} = 0\quad (i,\, j = \mathrm{m,\,s,\,a}) \tag{1}$$

$$\frac{\partial(\rho_b C_b^{H_2O})}{\partial t} + \sum_i^{m,s,a}\nabla\cdot\left[\rho_i\phi_i C_i^{H_2O}\boldsymbol{V}_i\right] = 0 \tag{2}$$

$$\nabla^4\psi_s = 0\ \text{ and }\ \boldsymbol{V}_s = (u_s, v_s) = \left(\frac{\partial\psi_s}{\partial z}, -\frac{\partial\psi_s}{\partial x}\right) \tag{3}$$

$$\boldsymbol{V}_m = \boldsymbol{V}_s \tag{4}$$

$$\boldsymbol{V}_a = \boldsymbol{V}_s - \frac{k_{\phi_a}}{\phi_a\eta_a}\left[\eta_s\nabla^2\boldsymbol{V}_s + (1-\phi_a)\Delta\rho_a g\boldsymbol{z}\right]$$

$$\text{and}\ \ k_{\phi_a} = \frac{R^2\phi_a^n}{B} \tag{5}$$

$$\left[\sum_i^{m,s}(\phi_i\rho_i C_p^i) + T\Delta S\frac{(\partial\phi_m\rho_m)}{\partial T}\right]\frac{\partial T}{\partial t}$$

$$= K\nabla^2 T - \sum_i^{m,s}(\phi_i\rho_i C_p^i\boldsymbol{V}_i\cdot\nabla T - T\phi_i\alpha_i\boldsymbol{V}_i\cdot\nabla P$$

$$- T\Delta S)\frac{\partial(\phi_m\rho_m)}{\partial(C_b^{H_2O})}\frac{\partial(C_b^{H_2O})}{\partial t} - T\Delta S\nabla\cdot(\phi_m\rho_m\boldsymbol{V}_m) \tag{6}$$

where, for phase i (m = melt, s = solid, a = aqueous fluid), ρ_i is the density, ϕ_i is the volume fraction, $\boldsymbol{V}_i$ is the velocity vector, $\Gamma_{j\to i}$ represents the rate of mass transfer from phase j to i (e.g. $\Gamma_{s\to m}$ is the melting rate), $C_i^{H_2O}$ is the concentration of H_2O, and t is the time. In Eq. 2 for the local bulk system (b = m + s + a), ρ_b is the average density and $C_b^{H_2O}$ is the average concentration of H_2O. Although the aqueous fluid dissolves a significant amount of silicate components in the pressure and temperature range of interest [17,18], $C_a^{H_2O}$ (aqueous fluid) is assumed to be 1. In Eq. 3 for the solid flow, ψ_s is the stream function, u_s and v_s are the horizontal and vertical velocity components. In Eq. 5 for the flow of aqueous fluid, k_{ϕ_a} is the permeability, η_a is the viscosity, $\Delta\rho_a$ is $\rho_s - \rho_a$, g is the acceleration due to gravity, $\boldsymbol{z}$ is the unit vector of the vertical coordinate, R is the radius of the solid grain, and n and B are constants ($n = 3$ and $B = 10^3$ are assumed [26]). Since the fraction of aqueous fluid is small, it is assumed that the flow of aqueous fluid does not affect the flow of solid and melt, and that the pressure of solid and melt is constant with time. The viscous or elastic resistance of the solid and melt to the volume change is neglected in Eq. 5. This assumption is inadequate for describing the vicinity of a porosity shock [27], but is probably useful to estimate the approximate fluid fluxes. In Eq. 6, S_i is the entropy,

C_P^i is the heat capacity at constant pressure, α_i is the thermal expansion coefficient, $\Delta S_{s\to m}$ is the entropy change associated with melting, and K is the thermal conductivity. In Eq. 6, energy transported by the aqueous fluid and energy for phase transformation related to the aqueous fluid are neglected. Also instantaneous local thermal equilibrium between the phases present, no viscous dissipation of energy, and no entropy change of each phase associated with compositional changes are assumed.

These equations are nondimensionalized using $(x, z) = (x', z')d$, $t = t'd^2\kappa^{-1}$, $\Psi_s = \Psi_s' u_0 d_0$, $\boldsymbol{V}_i = \boldsymbol{V}_i' u_0$, $\Gamma_{s\to m} = \Gamma'_{s\to m}\rho_m\kappa d^{-2} = \Gamma'_{s\to m}K(C_P^m)^{-1}d^{-2}$, $P = P'\rho g d$, and $T = (T' + T_0')\Delta T$, where the primes indicate the nondimensional variables, d is the vertical scale of the investigated region, d_0 is the thickness of subducting slab, T_0 is the reference temperature, and ΔT is the reference temperature interval. Assuming $\rho_b = \rho_m = \rho_s =$ constant (ρ), $\alpha_m = \alpha_s =$ constant (α) and $C_P^m = C_P^s =$ constant (C_P), we obtain the following nondimensional variables:

$$A_1 = \frac{u_0 d}{\kappa},\quad A_2 = \frac{R^2\eta_s}{\eta_a B d^2},\quad A_3 = \frac{R^2\Delta\rho_a g}{\eta_a B u_0},$$
$$A_4 = \frac{\Delta S}{C_P},\quad A_5 = \frac{\alpha g d}{C_P} \tag{7}$$

A_1 scales the transportation of mass or energy associated with advection, A_2 and A_3 scale the fluid flow driven by pressure gradient due to the solid flow and the density contrast, respectively, A_4 measures the impact of melting–solidification on the energy balance, and A_5 is the dissipation number. Although the calculations for energy conservation are based on the dimensional phase relationships (Figs. 1–3), scaling is useful for estimating contributions of each term. When $u_0 = 2\times10^{-9}$ m s^{-1}, $d = 2.5\times10^5$ m, $\kappa = 1.0\times10^{-6}$ m^2 s^{-1}, $R = 1.0\times10^{-3}$ m, $\eta_s = 10^{21}$ Pa s, $\eta_a = 10^{-3}$ Pa s, $B = 10^3$, $\Delta\rho_a = 2.3\times10^3$ kg m^{-3} [28], $g = 9.8$ m s^{-2}, $\Delta S = 3.5\times10^2$ J kg^{-1} K^{-1}, $C_P = 1.2\times10^3$ J kg^{-1} K^{-1}, and $\alpha = 2.4\times10^{-5}$ K^{-1}, then $A_1 = 4.0\times10^2$, $A_2 \sim 1.6\times10^4$, $A_3 \sim 1.1\times10^7$, $A_4 = 0.29$, and $A_5 = 4.9\times10^{-2}$. The values allow us to illustrate a rough configuration of the system: heat is transported mainly by advection of the solid, which is modified by conduction and melting–solidification. Migration of the aqueous fluid is controlled by buoyancy upwards when ϕ_a is greater than $\sim3\times10^{-4}$, and is controlled by the solid flow when ϕ_a is smaller than $\sim3\times10^{-4}$. As will be shown later, the representative fraction of the aqueous fluid in the mantle wedge is likely to be larger than this critical value.

These equations are solved numerically with a finite difference scheme. A cross-sectional area of subduction zones of a 250 × 250 km box is divided into a 125 × 125 regular grid (Fig. 5). The oceanic crust which initially contains $C_{oc}^{H_2O} = 6$ wt% H_2O [6] is subducted from the trench (top left corner of the box) with a subduction angle of 45°, and undergoes dehydration reactions as in Fig. 4, to generate aqueous fluids. If these fluids ascend in the mantle wedge over a lateral interval w, the representative fluid fraction is expressed by:

$$\phi_a^0 = \left(\frac{d_{oc}C_{oc}^{H_2O}}{A_3 w\dfrac{\rho_a}{\rho_s}}\right)^{1/3} \tag{8}$$

where d_{oc} is the thickness of oceanic crust, and v_a is the upward velocity of the aqueous fluid. When $d_{oc} = 7.0\times10^3$ km, $w = d$, and giving other parameter values as in the previous paragraph, $\phi_a^0 = 3.5\times10^{-3}$. This estimate is rather insensitive to the parameter value A_3 (constant describing the permeable flow) which is not well constrained. As will be shown in the results of full numerical calculations, w is smaller than d because of a limited interval of dehydration reactions to form a column of ascending aqueous fluid, while the oceanic crust loses a significant amount of H_2O at shallow depths, before it starts to supply H_2O to the mantle wedge. The effects of these factors on ϕ_a^0 tend to cancel each other out. Also the solid and melt can transport H_2O to decrease ϕ_a^0. For these reasons, both simple scaling in Eq. 8 and the full calculations give a similar value for ϕ_a^0.

5. Results and discussion

Fig. 5a shows the results for subduction of an old cold slab (age 130 Myr) with subduction velocity ~6 cm/year such as in northeast Japan. Based on a global thermal model [10], a potential temperature of ~1250°C for the mantle wedge is assumed, which is

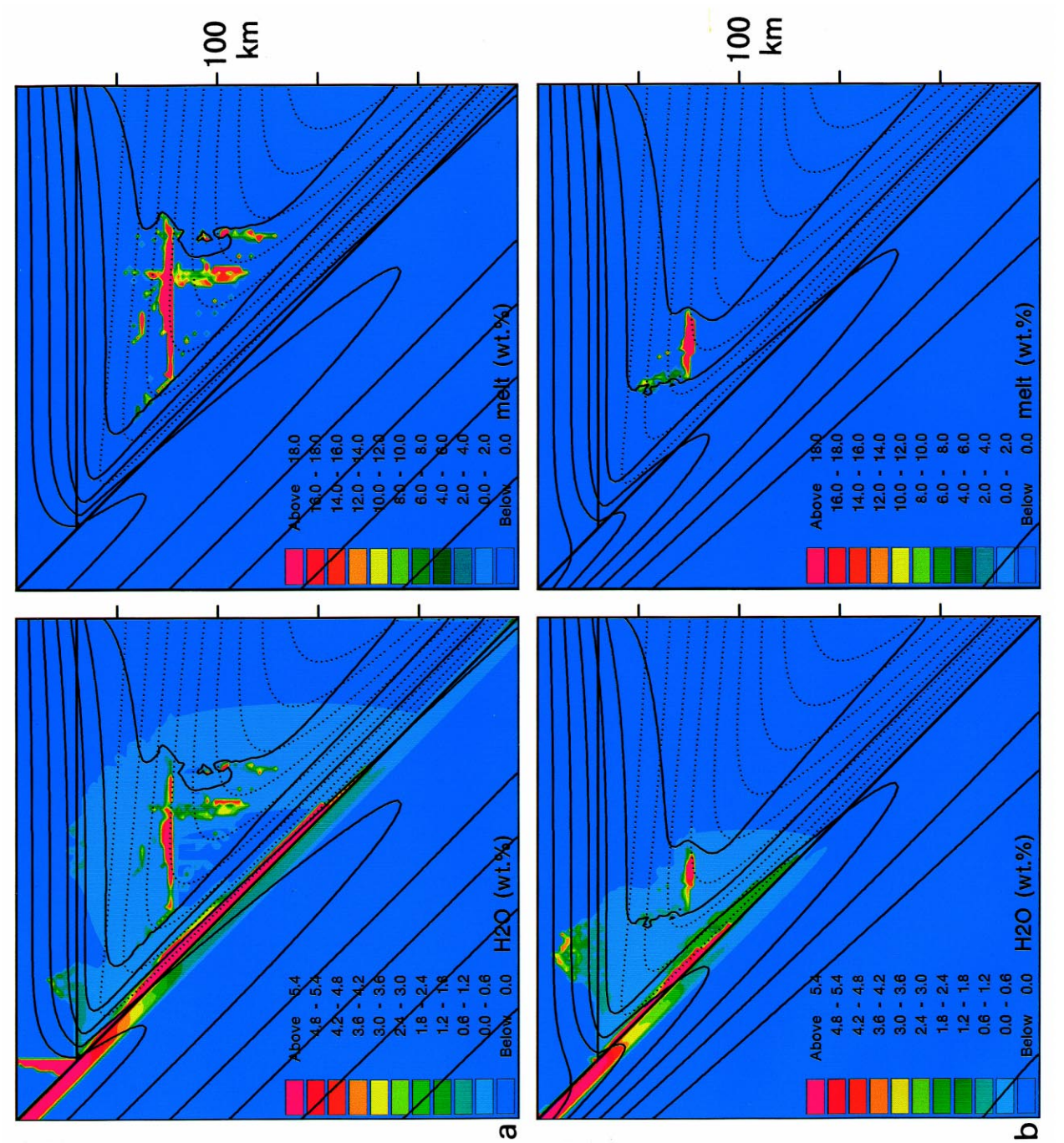
100 km
Above 18.0
16.0 - 18.0
14.0 - 16.0
12.0 - 14.0
10.0 - 12.0
8.0 - 10.0
6.0 - 8.0
4.0 - 6.0
2.0 - 4.0
0.0 - 2.0
Below 0.0
melt (wt.%)
Above 5.4
4.8 - 5.4
4.2 - 4.8
3.6 - 4.2
3.0 - 3.6
2.4 - 3.0
1.8 - 2.4
1.2 - 1.8
0.6 - 1.2
0.0 - 0.6
Below 0.0
H2O (wt.%)
a
b

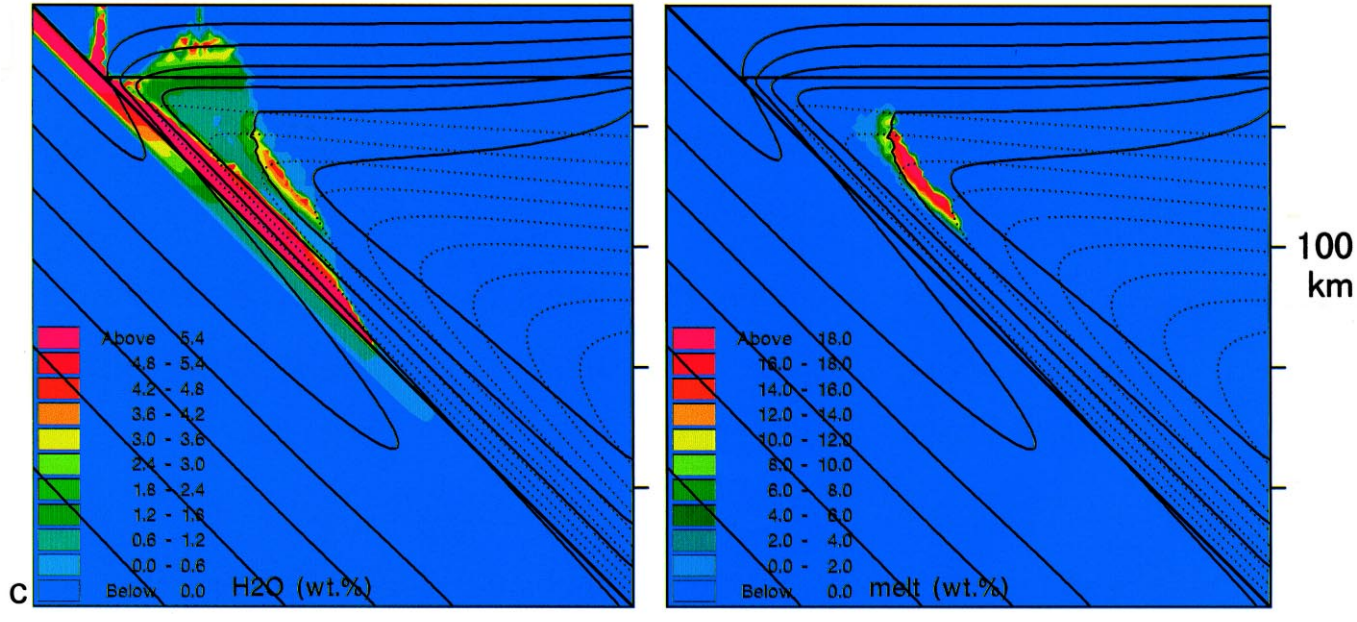

Fig. 5. Distribution of H_2O (left) and melt (right). (a) For a relatively cold slab (age, t_s, of 130 Myr) with a constant subduction velocity, u_0, of 2×10^{-9} m s^{-1} (~6 cm/year). A cross-sectional area of 250 × 250 km region with a fixed crust of 30 km thick is divided into a 125 × 125 regular grid for numerical calculations, with a finer triangular grid at the slab–wedge interface and at the bottom of the slab for preventing artificial diffusion of H_2O. The thickness of rigid slab, d_s, can be defined as 2.32 $(\kappa t_s)^{1/2}$ where κ is the thermal diffusivity [39]. If $\kappa = 10^{-6}$ m^2 s^{-1}, $d_s = 1.49 \times 10^5$ m. In both the oceanic side (lower left corner) and the mantle wedge (upper right) of the rigid slab, the solid flow is assumed to be described by analytic corner flow solutions of incompressible fluid with constant viscosity [24]. The dotted lines in the mantle wedge indicate the stream lines. The thermal boundary conditions are as follows: a surface temperature of 273 K; an error function gradient for the plate age of 130 Myr and an adiabatic gradient underneath for the oceanic side boundary; a linear gradient within the crust and within a thermal boundary layer of 12 km beneath the crust to produce the surface heat flux of 0.115 W/m^2, and an adiabatic gradient underneath for the arc side boundary, which gives the potential temperature ~1250ºC; zero heat flux at the bottom boundary. The solid lines indicate the isothermal contours with a 200-K interval. A steady geothermal structure for H_2O-free subduction of the slab was assumed for an initial condition where no melt exists, then the slab with 6 wt% H_2O started to subduct. The elapsed time for this snapshot is 7.1 Myr. (b) For a hot slab (age of 10 Myr) with a constant subduction velocity, u_0, of 2×10^{-9} m s^{-1} (~6 cm/year). The thickness of rigid slab is $d_s = 4.12 \times 10^4$ m. The other conditions are the same as in (a). The elapsed time for this snapshot is 4.1 Myr. (c) For a case involving disequilibrium transportation of H_2O. A small portion of the aqueous fluid (8% of the aqueous fluid present in each local system) is assumed to be isolated chemically in the local system. Consequently, once the aqueous fluid is produced, it can survive and continue to migrate even if the surrounding solid and melt are not saturated with H_2O. The other conditions are the same as in (a). The elapsed time for this snapshot is 2.9 Myr.

lower than that inferred from petrological constraints by up to 100ºC [29,30]. However, the following discussions on dehydration processes and migration of H_2O are not affected much by this ambiguity, since the temperature along the slab is rather insensitive to the wedge temperature [7].

The subducted oceanic crust, which initially contains 6 wt% H_2O mainly in chlorite, lawsonite and amphibole, undergoes dehydration and produces aqueous fluids of total ~3 wt% at a depth of 50 km. If the network of the aqueous fluid is achieved, the fluid can ascend, following Eq. 5. As it enters the mantle wedge, a layer of serpentinite thinner than the oceanic crust is formed to accommodate all H_2O released, since it can absorb ~8 wt% H_2O. Although serpentine breaks down where this layer thickens to reach an inner wedge region of above 600ºC, nearly all the H_2O is brought down to ~150 km (5 GPa), due to low temperatures along the slab. Chlorite is also stable up to ~5 GPa (Fig. 2).

At ~150 km depth, serpentine and chlorite break down to form a vertical column through which H_2O is transported by a 'fluid'. The fluid may contain a significant amount of silicate components, and could be either aqueous solution or H_2O-rich melt, as has been discussed. When the fluid reaches a depth of ~80 km, the temperature of the system exceeds the practical solidus temperature to cause significant melting. The *P–T* condition is close to the cusp of the H_2O-undersaturated solidus around 2.5 GPa (Fig. 1). Then H_2O is absorbed into the melt and transported towards the trench side along the solid stream lines, resulting in a horizontal melting layer. This is an artifact due to the assumption of no melt segregation. Effects of segregation will be discussed later.

Fig. 5b shows the results for subduction of a relatively hot slab (age about 10 Myr), with the same parameters for the other conditions as in Fig. 5a. Due to the higher temperature along the slab, the relevant dehydration reactions occur at shallower depths than in Fig. 5a. Serpentine in the wedge just above the slab breaks down at 700ºC and 90 km, and chlorite breaks down at about 800ºC and 120 km. Consequently, hydrous columns are formed at shallower levels, closer to the trench, whereas the flux of H_2O through the column is similar to that in Fig. 5a, initiating melting at a similar depth.

Fig. 6 schematically shows a representative transportation path of H_2O in Fig. 5a and b. Aqueous fluid released from the oceanic crust at point A migrates upward to point B where serpentine and chlorite are formed. Between points B and C, amphibole and a small amount of serpentine break down to release H_2O. Although this small amount of H_2O can not contribute much to melting beneath the volcanic front, the fluid may transport key materials, such as ^{10}Be and U–Th series nuclides that characterize subduction zone magmas. In this case, the circulation time of fluids inferred from these isotopes may not represent that of the majority of H_2O, but does correspond to the shortcut.

Around point C, dehydration of serpentine and chlorite occurs, and H_2O ascends towards a higher temperature region by aqueous solution or H_2O-rich melt. At point D, the temperature exceeds the practical solidus to cause extensive melting. Then, in this model without melt segregation, H_2O is transported horizontally towards the trench side, being hosted by melt and solid. If melt segregation occurs, H_2O and melt will be extracted upwards, and the packet consisting of residual melt and solid becomes depleted in H_2O along the streamline. In any case, the packet starts to descend at point E (beneath around the volcanic front), where either compression melting [8–10] or compression solidification occurs depending on the amount of H_2O.

For a higher geothermal gradient along the slab, points A, C, and the fluid columns occur at shallower levels, closer to the trench, whereas the depth of point D and the location of point E are nearly fixed, although the melting region shrinks on the backarc side. This is because the flux of H_2O from C to D, hence the practical solidus, as well as the flow pattern of the solid, are similar for various slab ages. Assuming that the melt segregates vertically, this constant position of point E may explain why the location of the volcanic front seems not to change systematically for a given subduction angle with different slab ages and geothermal gradients along the slab (e.g. Aleutian and Mexico [1]).

Fig. 7 shows the representative *P–T* paths of H_2O in Fig. 5a and b, which confirms that breakdown of serpentine and chlorite leads to formation of the fluid columns and melting, and that, although the depth of the fluid column is decreased for a

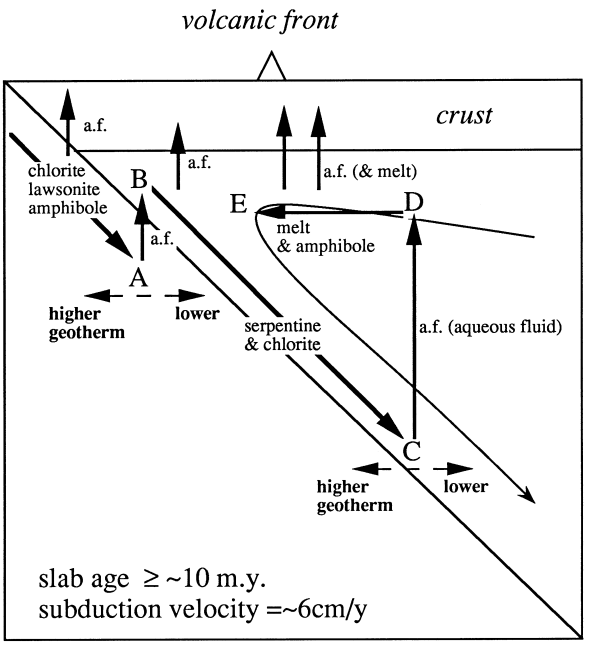

Fig. 6. Schematic figure summarizing Fig. 5a and b, showing the main phases hosting H_2O along the transportation paths. The meanings of points A to E are explained in the text.

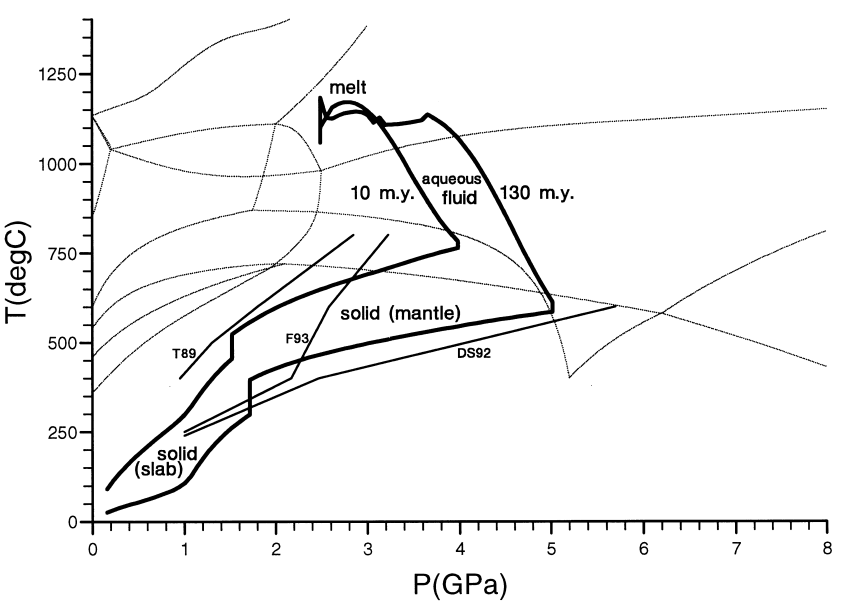

Fig. 7. Representative transportation paths of H_2O in *P–T* space with the phase relationships of hydrous peridotite from Fig. 2 (dotted lines). The thick line labelled 130 Myr corresponds to Fig. 5a, and 10 Myr corresponds to Fig. 5b. The solid lines *T89*, *F93* and *DS92* represent the temperature at the slab–wedge interface from Fig. 2 (model TMJ) of Ref. [3], Fig. 2 ($u_0 = 4$ cm/year, and subduction angle of 30 to 60 degrees) of Ref. [25], and Fig. 5b ($u_0 = 4.5$ cm/year, and subduction angle of 60° of Ref. [7], respectively.

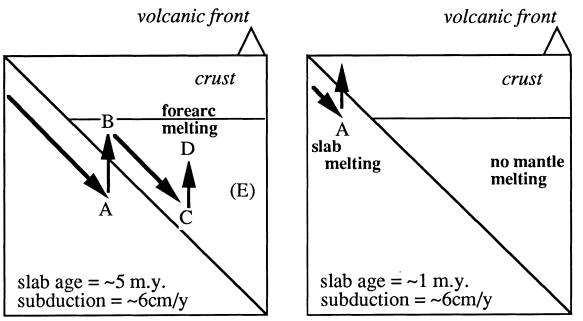

Fig. 8. The main paths of aqueous fluid for very young and hot subducting slabs (∼5 Myr and ∼1 Myr). The fluid generation and migration have not been actually calculated for these cases due to numerical difficulties, but are illustrated based on the thermal structures as have been calculated for Fig. 5, with different thermal boundary conditions for younger slabs. The points *A* to *E* have the same meanings as in Fig. 6.

younger subducting slab, a similar melting condition is achieved for both cases. If the geothermal gradient is further increased for hot slabs (e.g. age $<$ 10 Myr when $u_0 \sim 6$ cm/year), then different melting regimes will occur as is shown in Fig. 8: points A to D are shifted trenchward, and the fluid column C–D is located on the trench side of point E of Fig. 6. Therefore, melting can occur only in the forearc region with a temperature above the hydrous solidus of peridotite (minimum 970ºC). If the slab is further young and hot (e.g. ∼1 Myr when $u_0 \sim 6$ cm/year), before it supplies H_2O to the mantle wedge, the slab itself will melt where the temperature exceeds the hydrous solidus of basalt (minimum 650ºC at around 1 GPa [22]).

The discussion so far assumes chemical equilibrium. If disequilibrium transportation of aqueous fluid occurs (e.g. through fractures [31]), the aqueous fluid can exist even when solid and melt are not saturated with H_2O. Fig. 5c shows the results in which 10 wt% of the fluid present is assumed to be chemically isolated in the local system. This causes leakage of a significant amount of H_2O from the serpentinite layer which should act as nearly perfect H_2O-absorber if chemical equilibrium is achieved. Consequently, extensive melting occurs in the forearc region. In most subduction zones, this is not the case, and the serpentinite layer is expected to act as the effective H_2O-absorber.

There is an argument that dihedral angles between the aqueous fluid and the solid are large in the subducting slab, and that the fluid network as a flow path is not formed at $\leq$∼1 GPa [32]. At greater depths where the dihedral angle decreases, the network may be formed to allow the fluid to escape from the slab. In this case, again the serpentinite layer just above the slab can act as an effective H_2O-absorber.

The models presented in this paper simply use the phase relationships for peridotitic and basaltic systems, which are already known, and calculates consequential phase transformation including melting. However, essential differences from the previous studies exist in several aspects. The following arguments clarify the differences, which also summarizes the discussion so far. Tatsumi [3] argued that amphibole in the downward flow of the mantle wedge breaks down to release H_2O, which ascends vertically as a fluid to cause extensive flux melting and formation of a volcanic front. In his estimates, a very large dT/dP for the geotherm along the slab is selected from thermal models of subduction zones (e.g. [33]), in which serpentine and chlorite are unstable at pressures greater than 2.5 to 3 GPa (Fig. 7). Consequently, melting in the forearc region occurs as in Fig. 8 for a hot slab, which is not the case in most subduction zones with normal arc magmatism as in Fig. 5 for a colder slab (e.g. $\geq$∼10 Myr age when $u_0 \sim 6$ cm/year).

Recent numerical modelling of thermal structures in subduction zones [7,10], including this study, predicts a similar temperature along the slabs of $\geq$∼10 Myr age and $u_0 \sim 2$ to 9 cm/year (Fig. 7), which is significantly lower than that selected in Ref. [3]. The exception is a model incorporating temperature-dependent viscosity [25], in which the slab–wedge interface with a thinner thermal boundary layer can be heated up to 800ºC at $\leq$3 GPa. Although the viscosity must depend on the temperature, this model [25] results in forearc melting without normal arc magmatism. It is not clear at present whether other factors (e.g. stress-dependent viscosity) play important roles and need be introduced into the models.

Davies and Stevenson [7] argued that H_2O released from amphibole reacts with peridotites during its ascent to form amphibole again and is brought down by the solid flow parallel to the slab. By repeating this process, they showed that H_2O can travel over a significant lateral distance to a potential melt-

ing region. This happens in the current model at a region around points B and E. However, the amount of H_2O transported by this process is small, and the serpentinite layer just above the slab primarily controls the H_2O-budget, which has not been considered in Ref. [7].

Schmidt and Poli [6] clarified the subsolidus phase relationships in the basaltic and peridotitic systems, on which a significant part of this study is based. Schmidt and Poli [6] discussed that the dehydration reactions occur rather continuously and depend on the thermal structure. They assume that the aqueous fluid ascends to mantle wedge of high temperature, neglecting the interaction with the mantle wedge to form hydrous minerals such as serpentine and chlorite (i.e. disequilibrium transportation). They could not attribute the formation of the volcanic front to a unique major dehydration event, and instead proposed that the thermal structure in the mantle wedge controls the location of the volcanic front. The case in Fig. 5c corresponds to what they proposed, in which case extensive melting must occur in the forearc region.

6. Summary

A numerical model which describes generation and migration of aqueous fluid and subsequent chemical reactions with the convecting solid in subduction zones, including melting, has been presented. A serpentinite layer with chlorite just above the slab plays a primary role in absorbing H_2O expelled from the slab and carries it down by up to 150 km. Both the position of the breakdown of serpentine and chlorite and the position of the fluid column depend on the thermal structure. However, the lateral extent on the trench side and the initial depth of the melting region are nearly fixed, because the flux of H_2O and the flow pattern of the solid are similar for different slab ages. Exceptionally, for very young slabs (e.g. $\ll$10 Myr when $u_0 \sim 6$ cm/year), the melting regime switches to forearc and slab melting. Disequilibrium transportation of aqueous fluid leads to extensive melting in the forearc region, which suggests that absorption of H_2O by serpentine and chlorite just above the slab is required for most subduction zones. Further studies with various subduction parameters, together with consideration for melt segregation processes, are required to compare the model results with the observed distribution and chemistry of arc magmas.

Acknowledgements

The author would like to thank M. Schmidt for his extensive discussions at Tokyo Institute of Technology and providing a preprint of his paper, and S. Maruyama, K. Hirose, T. Sumita, C. Richardson and T. Tanaka for discussions and help, and K. Hirose, Y. Tatsumi and an anonymous referee for reviews. ***[FA]***

References

[1] J.B. Gill, Orogenic Andesites and Plate Tectonics, Springer-Verlag, Berlin, 1981.
[2] Y. Tatsumi, S. Eggins, Subduction Zone Magmatism, Blackwell, Cambridge, 1995.
[3] Y. Tatsumi, Migration of fluid phases and genesis of basalt magmas in subduction zones, J. Geophys. Res. 94 (1989) 4697–4707.
[4] S.M. Peacock, Fluid processes in subduction zones, Science 248 (1990) 329–337.
[5] A.B. Thompson, Water in the Earth's upper mantle, Nature 358 (1992) 295–302.
[6] M.W. Schmidt, S. Poli, What causes the position of the volcanic front? Experimentally based water budgets for dehydrating slabs and consequences for arc magma generation, Earth Planet. Sci. Lett. 1997, submitted.
[7] J.H. Davies, D.J. Stevenson, Physical model of source region of subduction zone volcanics, J. Geophys. Res. 97 (1992) 2037–2070.
[8] H. Iwamori, Importance of compression melting in subduction zones, Proc. Jpn. Acad. Ser. B 72 (1996) 168–173.
[9] H. Iwamori, Compression melting in subduction zones, Terra Nova 9 (1997) 9–13.
[10] H. Iwamori, Heat sources and melting in subduction zones, J. Geophys. Res. 102 (1997) 14803–14820.
[11] D.H. Green, Experimental melting studies on a model upper mantle composition at high pressure under water-saturated and water-undersaturated conditions, Earth Planet. Sci. Lett. 19 (1973) 37–53.
[12] B.O. Mysen, A.L. Boettcher, Melting of hydrous mantle, I: Phase relations of natural peridotite at high pressures and temperatures with controlled activities of water, carbon dioxide, and hydrogen, J. Petrol. 16 (1975) 520–548.
[13] M.E. Wallance, D.H. Green, An experimental determination of primary carbonatite magma composition, Nature 335 (1988) 343–346.
[14] S. Foley, High-pressure stability of the fluor- and hydroxy-

endmembers of pargasite and K-richterite, 55, 2689–2694, 1991.
[15] T. Inoue, H. Sawamoto, High pressure melting of pyrolite under hydrous condition and its geophysical implications, in: Y. Soyono, M.H. Manghnani (Eds.), High-Pressure Research: Application to Earth and Planetary Sciences, Terrapub, Tokyo and AGU, Washington, D.C., 1992, pp. 323–331.
[16] I. Kushiro, Y. Syono, S. Akimoto, Melting of a peridotite nodule at high pressures and high water pressures, J. Geophys. Res. 73 (1968) 6023–6029.
[17] Y. Nakamura, I. Kushiro, Composition of the gas phase in Mg_2SiO_4–SiO_2–H_2O at high pressures, Carnegie Inst. Washington Yearb. 73 (1974) 266–268.
[18] T. Fujii, K. Mibe, A. Yasuda, Magma ocean did not exist?, Kagaku 67 (1997) 179–183.
[19] T. Kawamoto, J. Holloway, Melting temperature and partial melt chemistry of H_2O–saturated mantle peridotite to 11 gigapascals, Science 276 (1997) 240–243.
[20] K. Hirose, Melting experiments on lherzolite KLB-1 under hydrous conditions and generation of high-magnesian andesitic melts, Geology 25 (1997) 42–44.
[21] H. Iwamori, D. McKenzie, E. Takahashi, Melt generation by isentropic mantle upwelling, Earth Planet. Sci. Lett. 134 (1995) 253–266.
[22] S. Poli, The amphibolite–eclogite transformation: an experimental study on basalt, Am. J. Sci. 293 (1993) 1061–1107.
[23] S. Ono, Water Transport in Subduction Zones, Ph.D. thesis, University of Tokyo, Tokyo, 1997, 101 pp.
[24] G.K. Batchelor, An Introduction to Fluid Dynamics, Cambridge University Press, Cambridge, 1967, 615 pp.
[25] Y. Furukawa, Magmatic processes under arcs and formation of the volcanic front, J. Geophys. Res. 98 (1993) 8309–8319.
[26] D. McKenzie, The generation and compaction of partially molten rock, J. Petrol. 25 (1984) 713–765.
[27] M. Spiegelman, Flow in deformable porous media, II: Numerical analysis — the relationship between shock waves and solitary waves, J. Fluid. Mech. 247 (1993) 39–63.
[28] H.C. Helgeson, D.H. Kirkham, Theoretical prediction of the thermodynamic behaviour of aqueous electrolytes at high pressures and temperatures, I: Summary of the thermodynamic/electrostatic properties of the solvent, Am. J. Sci. 274 (1974) 1089–1198.
[29] Y. Tatsumi, M. Sakuyama, Y. Fukuyama, I. Kushiro, Generation of arc basalt magmas and thermal structure of the mantle wedge in subduction zones, J. Geophys. Res. 88 (1983) 5815–5825.
[30] M.B. Baker, T.L. Grove, R. Price, Primitive basalts and andesites from the Mt. Shasta region, N. California: products of varying melt fraction and water content, Contrib. Mineral. Petrol. 118 (1994) 111–129.
[31] H. Iwamori, A model for disequilibrium mantle melting incorporating melt transport by porous and channel flows, Nature 366 (1993) 734–737.
[32] B.E. Watson, J.M. Brenan, Fluids in the lithosphere, part 1: experimentally-determined wetting characteristics of CO_2–H_2O fluids and their implications for fluid transport, hostrock physical properties and fluid inclusion formation, Earth Planet. Sci. Lett. 85 (1987) 497–515.
[33] M.N. Toksöz, J.W. Minear, B.R. Julian, Temperature field and geophysical effects of a downgoing slab, J. Geophys. Res. 76 (1971) 1113–1138.
[34] A.V. Menner, T. Dunn, Amphibole and phlogopite stability in an initially amphibole-bearing spinel peridotite under water-undersaturated conditions: 1 to 2.5 GPa, Eos Fall Mtg. (1995) F697.
[35] T. Inoue, Effect of water on melting phase relations and melt composition in the system Mg_2SiO_4–$MgSiO_3$–H_2O up to 15 GPa, Phys. Earth Planet. Inter. 85 (1994) 237–263.
[36] T. Sumita, T. Inoue, Melting experiments and thermodynamic analyses on silicate–H_2O systems up to 12 GPa, Phys. Earth Planet. Inter. 96 (1996) 187–200.
[37] W.H. Press, S.A. Teukolsky, W.T. Vetterling, B.P. Flannery, Numerical Recipes, Cambridge Univ. Press, Cambridge, 1992, 963 pp.
[38] J. Braun, M. Sambridge, A numerical method for solving partial differential equations on highly irregular evolving grids, Nature 376 (1995) 655–660.
[39] D.L. Turcotte, G. Schubert, Geodynamics, Wiley, New York, 1982.